

Primordial non-Gaussianity – the effects of relativistic and wide-angle corrections to the power spectrum

Sêcloka L. Guedezounme^{1,a}, Sheean Jolicoeur^{2,b},
Roy Maartens^{1,3,4,c}

¹Department of Physics & Astronomy, University of the Western Cape, Cape Town 7535, South Africa

²Department of Physics, Stellenbosch University, Matieland 7602, South Africa

³Institute of Cosmology & Gravitation, University of Portsmouth, Portsmouth PO1 3FX, United Kingdom

⁴National Institute for Theoretical & Computational Sciences (NITheCS), Cape Town 7535, South Africa

E-mail: ^aseclokaguedezounme@gmail.com, ^bjolicoeursheean@gmail.com,
^croy.maartens@gmail.com

Abstract. Wide-angle and relativistic corrections to the Newtonian and flat-sky approximations are important for accurate modeling of the galaxy power spectrum of next-generation galaxy surveys. In addition to Doppler and Sachs-Wolfe relativistic corrections, we include the effects of lensing convergence, time delay and integrated Sachs-Wolfe. We investigate the impact of these corrections on measurements of the local primordial non-Gaussianity parameter f_{NL} , using two futuristic spectroscopic galaxy surveys, planned for SKAO2 and MegaMapper. In addition to the monopole, we include the quadrupole of the galaxy Fourier power spectrum. The quadrupole is much more sensitive to the corrections than the monopole. The combination with the quadrupole improves the precision on f_{NL} by $\sim 40\%$ and $\sim 60\%$ for SKAO2 and MegaMapper respectively. Neglecting the wide-angle and relativistic corrections produces a shift in f_{NL} of $\sim 0.1\sigma$ and $\sim 0.2\sigma$ for SKAO2 and MegaMapper. The shift in f_{NL} is very sensitive to the magnification bias and the redshift evolution of the comoving number density. For these surveys, the contributions to the shift from integrated and non-integrated effects partly cancel. We point out that some of the approximations made in the corrections may artificially suppress the shift in f_{NL} .

Contents

1	Introduction	2
2	Relativistic and wide-angle power spectrum	4
3	Constraining local primordial non-Gaussianity	12
4	Bias on the estimate of f_{NL}	14
5	Conclusion	16
A	Multipoles of the non-integrated power spectrum	17
B	Derivation of the integrated correction to the power spectrum	19
C	MegaMapper functions	21
D	Additional contour plots	22

1 Introduction

Primordial non-Gaussianity (PNG) is a key probe of Inflation models that are assumed to generate the primordial perturbations – which in turn seed the cosmological fluctuations measured by cosmic microwave background (CMB) and large-scale structure surveys [1–3]. Among the various forms of PNG, the local type, parametrised by f_{NL} , is of primary importance due to its characteristic scale-dependent impact on galaxy clustering. This dependence makes large-scale structure an indispensable tool for constraining inflationary physics through precise measurements of f_{NL} .

The analysis of the galaxy power spectrum often relies on simplifying theoretical assumptions, such as the plane-parallel and Newtonian approximations. While sufficient for small-scale studies, such approximations fail to account for relativistic and wide-angle effects, which become increasingly significant on ultra-large scales – where the local PNG signal is strongest. The corrections include local effects (wide-angle, Doppler and Sachs-Wolfe) as well as integrated effects (lensing convergence, integrated Sachs-Wolfe and time-delay) [4–6]. Neglecting these effects risks introducing systematic biases in estimates of f_{NL} and other key cosmological parameters [7–11].

Incorporating these relativistic and wide-angle corrections is therefore essential to exploit the full potential of the galaxy power spectrum as a cosmological probe. Here we treat these effects as leading-order modifications to the standard Fourier galaxy power spectrum, in order to estimate their influence on f_{NL} estimation. This is particularly relevant for next-generation surveys, which aim to probe ultra-large scales with high precision. We consider two complementary futuristic surveys: the SKAO2 HI galaxy survey which covers redshift 0 to 2 [12], and the MegaMapper LBG survey, covering redshift 2 to 5 [13].

The bispectrum of CMB temperature anisotropies has delivered the current best measurement and 1σ constraint on local PNG [14]

$$f_{\text{NL}} = -0.9 \pm 5.1. \quad (1.1)$$

The CMB and dark matter power spectra are not sensitive to local PNG, but local PNG changes the power spectrum of biased tracers such as galaxies – by inducing a scale-dependent contribution to the linear clustering bias:

$$b \rightarrow b + b_{\text{ng}} \quad \text{where} \quad b_{\text{ng}}(z, k) = 3\delta_c [b(z) - 1] \frac{\Omega_{m0} H_0^2 (1 + z_{\text{in}}) D_{\text{in}}}{D(z)} \frac{f_{\text{NL}}}{T(k) k^2}. \quad (1.2)$$

Here $\delta_c = 1.686$ is the critical collapse overdensity, z_{in} is a redshift deep in the matter-dominated era, D is the matter growth factor (normalised to 1 at redshift $z = 0$) and $T(k)$ is the matter transfer function. In (1.2) we have used a simple universality relation. There are serious issues involved in this assumption (see e.g. [15–18]), but our focus here is on comparing models of the power spectrum and not on realistic modeling of scale-dependent bias. It is clear that the local PNG signal is non-negligible only on ultra-large scales, $k < k_{\text{eq}}$, where T asymptotes to 1. These are the scales where the standard galaxy power spectrum acquires wide-angle and relativistic corrections, which therefore need to be incorporated for an accurate measurement of f_{NL} .

If n_g is the comoving number density of galaxies, then the number density contrast $\delta_g = (n_g - \bar{n}_g)/\bar{n}_g$ in configuration space is $\delta_g(\mathbf{x}_a) = b_a \delta(\mathbf{x}_a)$ (see Figure 1), where b_a is the linear Gaussian bias at x_a and δ is the matter density contrast. The observed number density

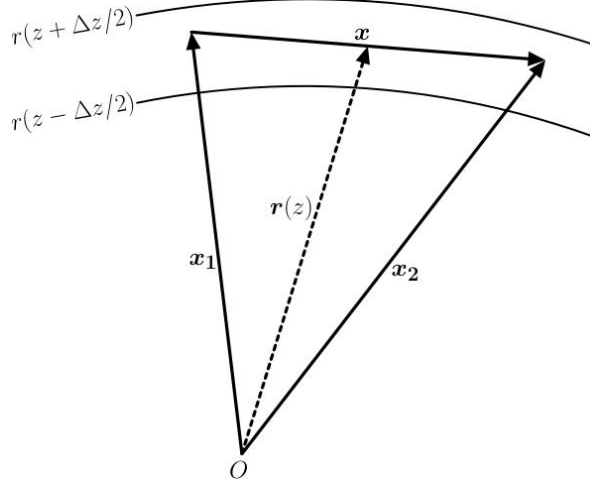


Figure 1. Geometry of the correlations.

contrast in redshift space is

$$\Delta_g(\mathbf{x}_a) = b_a \delta(\mathbf{x}_a) - \frac{1}{\mathcal{H}_a} \hat{\mathbf{x}}_a \cdot \nabla (\hat{\mathbf{x}}_a \cdot \mathbf{v}_a), \quad (1.3)$$

where the redshift dependence is implicit in $x_a(z)$ and b_a and \mathcal{H}_a (conformal Hubble rate) are evaluated at x_a . The galaxy peculiar velocity is \mathbf{v}_a and we have included only the dominant distortion term, in the standard Newtonian approximation. In Fourier space,

$$\Delta_g(x_a, \mathbf{k}_a) = \left(b_a + f_a \mu_a^2 \right) \delta(x_a, \mathbf{k}_a) \equiv \mathcal{K}^S(x_a, k_a, \mu_a) \delta(x_a, \mathbf{k}_a) \quad \text{with} \quad \mu_a = \hat{\mathbf{k}}_a \cdot \hat{\mathbf{x}}_a, \quad (1.4)$$

where \mathcal{K}^S is the Fourier kernel in the standard (S) approximation. In this approximation, the line-of-sight direction is fixed, using a flat-sky or plane-parallel assumption,

$$\hat{\mathbf{x}}_1 \approx \hat{\mathbf{x}}_2 \approx \hat{\mathbf{r}}, \quad (1.5)$$

where r is the comoving distance to the midpoint of the separation vector \mathbf{x} . In Equation 1.4, $f = -d \ln D / d \ln(1+z)$ is the linear growth rate. In order to ensure a physical matter power spectrum P on ultra-large scales, the density contrast should be the one measured in the matter rest-frame – i.e., δ should be in comoving gauge. Then the relativistic Poisson equation has the same form as the Newtonian Poisson equation:

$$\nabla^2 \Phi = \frac{3}{2} \Omega_m \mathcal{H}^2 \delta, \quad (1.6)$$

where Φ is the metric potential in Newtonian gauge:

$$ds^2 = a^2 \left[- (1 + 2\Phi) d\eta^2 + (1 - 2\Phi) d\mathbf{x}^2 \right]. \quad (1.7)$$

The standard power spectrum $P_g^S = (\mathcal{K}^S)^2 P$ implicitly assumes the plane-parallel approximation. Wide-angle corrections P_g^W arise from removing this assumption. The second type of correction to the standard power spectrum is from the relativistic effects introduced

by observing on the past lightcone. A theoretically complete treatment of wide-angle + relativistic effects is to use from the start the fully general 2-point correlation function (see e.g. [19–24]) or its angular harmonic transform (e.g. [4–6, 8, 25, 26]). These naturally incorporate all effects from observing the spherical sky on the past lightcone. An alternative, which exploits the computational advantages of the Fourier power spectrum, is to Fourier transform the 2-point correlation function which includes all relativistic and wide-angle effects (e.g. [27–29]) or transform to spherical Fourier-Bessel space (e.g. [30, 31]).

A simplification of the alternative approach is to include the wide-angle and relativistic effects as leading-order corrections to the standard Fourier spectrum (e.g. [32–34]):

$$P_g = P_g^S + P_g^{\text{corr}} \quad \text{with} \quad P_g^{\text{corr}} = P_g^{\text{NI}} + P_g^{\text{I}} \quad \text{up to} \quad \mathcal{O}\left[\frac{1}{k^2 r^2}, \frac{\mathcal{H}^2}{k^2}, \frac{1}{kr} \frac{\mathcal{H}}{k}\right], \quad (1.8)$$

Here NI denotes the leading-order non-integrated corrections: wide-angle (W) and relativistic Doppler and potential (R) effects – including the correlations $R \times S$, $W \times S$ and $R \times W$. This NI correction was derived in [32–34]. The integrated relativistic correction P_g^{I} in Equation 1.8 is the leading-order correction to P_g^S arising from lensing convergence (L), time-delay (TD) and integrated Sachs-Wolfe (ISW) effects.

2 Relativistic and wide-angle power spectrum

Figure 1 shows the configuration for 2-point correlations in a redshift bin, using the midpoint line of sight vector \mathbf{r} . Then the 2-point correlation function is $\xi(\mathbf{r}, \mathbf{x}) = \langle \Delta_g(\mathbf{x}_1, \mathbf{r}) \Delta_g(\mathbf{x}_2, \mathbf{r}) \rangle$, where $\mathbf{x} = \mathbf{x}_2 - \mathbf{x}_1$. The power spectrum $P_g(\mathbf{r}, \mathbf{k})$ is a local Fourier transform for each line of sight \mathbf{r} [32, 34]. The monopole and dipole of the non-integrated correction P_g^{NI} are derived in [34] and given in Appendix A for convenience.

Following [32], we include in P_g^{I} at leading order only the correlations of L+TD+ISW with the standard term, i.e., $(L+TD+ISW) \times S$. Qualitatively, in order to produce P_g^{I} , the integrated kernel \mathcal{K}^{int} is multiplied by the standard kernel \mathcal{K}^S , and then integrated from observer to source, with a radial weighting factor. This kernel is made up of three contributions:

$$\mathcal{K}^{\text{int}}(r, \tilde{r}, k, \mu) = \mathcal{K}^{\text{L}}(r, \tilde{r}, k, \mu) + \mathcal{K}^{\text{TD}}(r, \tilde{r}, k) + \mathcal{K}^{\text{ISW}}(r, \tilde{r}, k), \quad (2.1)$$

where $0 \leq \tilde{r} \leq r$ is the integration variable and r (at the source) is fixed for each integration. Note that at linear order the integration is along a background lightray, so that $\hat{\tilde{\mathbf{r}}} = \hat{\mathbf{r}}$ and \mathbf{n} , and therefore μ , remain constant.

The relativistic lensing convergence is defined in terms of the Laplacian on the 2-sphere, $\nabla_{\mathbf{n}}^2$, as follows [4, 35, 36]:

$$\kappa = \int_0^r d\tilde{r} \frac{\tilde{r}(r - \tilde{r})}{r} \tilde{\nabla}_{\mathbf{n}}^2 \tilde{\Phi} \quad \text{where} \quad \tilde{\nabla}_{\mathbf{n}}^2 = \nabla^2 - (\mathbf{n} \cdot \nabla)^2 + \frac{2}{\tilde{r}} \mathbf{n} \cdot \nabla. \quad (2.2)$$

Here and below, a tilde indicates that the quantity is evaluated at the background redshift \tilde{z} corresponding to \tilde{r} . The standard Newtonian approximation replaces $\tilde{\nabla}_{\mathbf{n}}^2$ by ∇^2 and uses the Poisson Equation 1.6 to eliminate Φ . This gives the dominant contribution to κ on scales $k > k_{\text{eq}}$:

$$\kappa_S = \frac{3}{2} \int_0^r d\tilde{r} \frac{\tilde{r}(r - \tilde{r})}{r} \tilde{\Omega}_m \tilde{\mathcal{H}}^2 \tilde{\delta}. \quad (2.3)$$

Here we focus on ultra-large scales, $k < k_{\text{eq}}$, so that we need to use the full expression [Equation 2.2](#). The lensing effect on galaxy number density contrast is given by the term

$$\Delta_g^{\text{L}} = 2(\mathcal{Q} - 1)\kappa, \quad (2.4)$$

where \mathcal{Q} is the magnification bias of the galaxy survey, which determines whether a galaxy is brightened or dimmed sufficiently by lensing to move above or below the flux cut. Using the relativistic κ in [Equation 2.2](#), this leads to the lensing kernel:

$$\mathcal{K}^{\text{L}}(r, \tilde{r}, k, \mu) = 3(\mathcal{Q} - 1)\tilde{\Omega}_m \tilde{\mathcal{H}}^2 \frac{\tilde{r}(r - \tilde{r})}{r} \left[1 - \mu^2 + 2i \frac{\mu}{\tilde{r}} \frac{G(r, \tilde{r})}{k} \right], \quad (2.5)$$

where the geometric weight factor is

$$G(r, \tilde{r}) = \frac{r + \tilde{r}}{2r}. \quad (2.6)$$

The remaining terms in [Equation 2.1](#) follow from the time-delay Δ_g^{TD} and integrated Sachs-Wolfe Δ_g^{ISW} contributions to the number counts [\[4, 6\]](#). These lead to the kernels [\[32\]](#):

$$\mathcal{K}^{\text{TD}}(r, \tilde{r}, k) = 6(\mathcal{Q} - 1) \frac{\tilde{\Omega}_m \tilde{\mathcal{H}}^2}{r} \left[\frac{G(r, \tilde{r})}{k} \right]^2, \quad (2.7)$$

$$\mathcal{K}^{\text{ISW}}(r, \tilde{r}, k) = 3 \left[\mathcal{E} - 2\mathcal{Q} + \frac{2(\mathcal{Q} - 1)}{r\mathcal{H}} - \frac{\mathcal{H}'}{\mathcal{H}^2} \right] \tilde{\Omega}_m \tilde{\mathcal{H}}^3 (\tilde{f} - 1) \left[\frac{G(r, \tilde{r})}{k} \right]^2, \quad (2.8)$$

where \mathcal{E} is the evolution bias of the galaxy survey, defined below.

The derivation of P_g^{I} is given in [\[32\]](#). For convenience we present our version of the derivation in [Appendix B](#). This leads to

$$P_g^{\text{I}}(r, k, \mu) = \int_0^r d\tilde{r} [\mathcal{J}(r, \tilde{r}, k, \mu) + \mathcal{J}^*(r, \tilde{r}, k, \mu)], \quad (2.9)$$

where

$$\mathcal{J}(r, \tilde{r}, k, \mu) = \frac{D(r)D(\tilde{r})}{G(r, \tilde{r})^3} \exp \left[-i \frac{\mu k}{G(r, \tilde{r})} (r - \tilde{r}) \right] \mathcal{K}^{\text{S}} \left(r, \frac{k}{G(r, \tilde{r})}, \mu \right) \mathcal{K}^{\text{int}*}(r, \tilde{r}, k, \mu) P_0 \left(\frac{k}{G(r, \tilde{r})} \right). \quad (2.10)$$

Here P_0 is the matter power spectrum at $z = 0$, and

$$\mathcal{K}^{\text{S}} \left(r, \frac{k}{G(r, \tilde{r})}, \mu \right) = b(r) + f(r)\mu^2 + b_{\text{ng}} \left(r, \frac{k}{G(r, \tilde{r})} \right). \quad (2.11)$$

In order to compute the integral [\(2.9\)](#), we use the Gauss-Legendre quadrature method and approximate the result as:

$$\int_{y_{\text{min}}}^{y_{\text{max}}} dy f(y) \approx \frac{y_{\text{max}} - y_{\text{min}}}{2} \sum_{i=1}^n w_i f \left(\frac{y_{\text{max}} - y_{\text{min}}}{2} \eta_i + \frac{y_{\text{max}} + y_{\text{min}}}{2} \right), \quad (2.12)$$

where η_i are the roots of the Legendre polynomial $\mathcal{L}_n(\eta)$ of degree n , which lie in the interval $[-1, 1]$, and w_i are the corresponding weights associated with each η_i :

$$\mathcal{L}_n(\eta_i) = 0, \quad w_i = \frac{2}{(1 - \eta_i^2) [\mathcal{L}'_n(\eta_i)]^2}. \quad (2.13)$$

The monopole and quadrupole of P_g^I involve a further integral; see [Appendix A](#) for some numerical details.

We consider two futuristic surveys: the Square Kilometer Array Phase 2 (SKAO2) HI galaxy survey [12] and the MegaMapper Lyman-Break Galaxy (LBG) [13] survey. The specifications of these surveys are summarised in [Table 1](#).

Table 1. Specifications of SKAO2 HI galaxy and MegaMapper LBG surveys.

Survey	Sky area [deg ²]	Redshift Range
SKAO2 HI galaxy	30,000	$0.1 \leq z \leq 2.0$
MegaMapper LBG	20,000	$2.0 \leq z \leq 5.0$

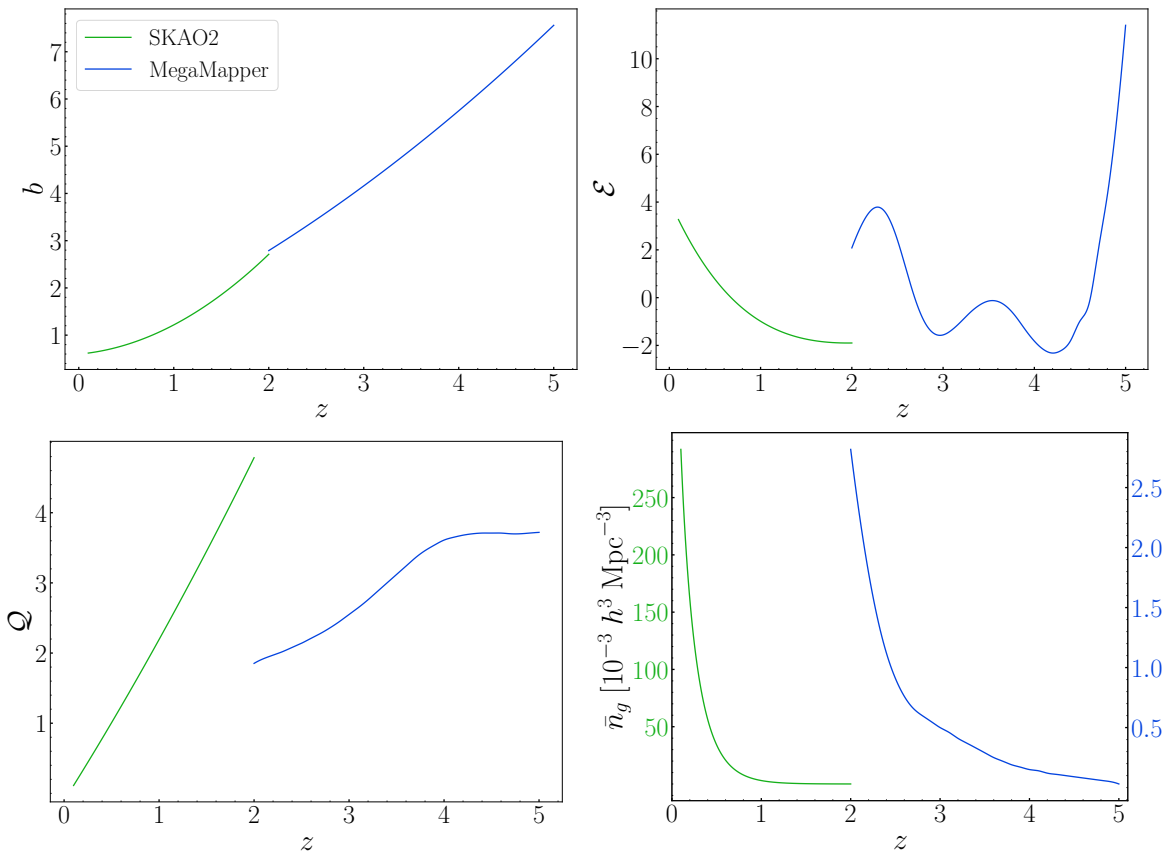


Figure 2. Galaxy clustering bias (*top left*), evolution bias (*top right*), magnification bias (*bottom left*) and number density (*bottom right*) for the SKAO2 HI galaxy and MegaMapper LBG samples.

[Appendix A](#) shows how the magnification bias Q and evolution bias \mathcal{E} enter the non-integrated relativistic corrections to the power spectrum monopole and quadrupole. It is clear from [Equation 2.5–Equation 2.8](#) that the integrated relativistic corrections also involve these two additional astrophysical parameters, which are defined as [12]:

$$Q = -\frac{\partial \ln \bar{n}_g}{\partial \ln L_c}, \quad (2.14)$$

$$\mathcal{E} = -\frac{\partial \ln \bar{n}_g}{\partial \ln(1+z)}, \quad (2.15)$$

where L_c is the luminosity cut corresponding to the survey flux cut. Then the Gaussian clustering bias b , the background number density \bar{n}_g , and \mathcal{Q} , \mathcal{E} for each survey are as follows (note that all fitting functions apply only over the redshift range of the survey).

- SKAO2 HI galaxy Survey:

$$b = b_0 (0.598 + 0.181z + 0.438z^2), \quad b_0 = 1.0, \quad (2.16)$$

$$\bar{n}_g = 0.298z^{-0.191} \exp(-4.599z) \quad h^3 \text{Mpc}^{-3}, \quad (2.17)$$

$$\mathcal{Q} = \mathcal{Q}_0 (-0.104 + 2.150z + 0.147z^2), \quad \mathcal{Q}_0 = 1.0, \quad (2.18)$$

$$\mathcal{E} = \mathcal{E}_0 (4.085 - 4.491z - 2.282z^2) \exp(-z), \quad \mathcal{E}_0 = 1.0. \quad (2.19)$$

The functions \bar{n}_g , \mathcal{Q} , \mathcal{E} are understood to be evaluated at the luminosity cut. Here the clustering bias b is a fit function derived from simulation data, based on a flux sensitivity threshold of $S_{\text{rms}} = 5 \mu\text{Jy}$ over the redshift range $0.1 \leq z \leq 2.0$, as described in Table A1 from [37]. The functions \bar{n}_g , \mathcal{Q} and \mathcal{E} are modelled as fits to simulation data, given in Table 2 of [12]. Uncertainties in the three biases are accounted for by the parameters b_0 , \mathcal{Q}_0 , \mathcal{E}_0 , each with fiducial value 1.

- MegaMapper LBG Survey:

$$b = b_0 (0.710 + 0.820z + 0.110z^2), \quad b_0 = 1.0, \quad (2.20)$$

is a fit from [38] to the values in [13]. The values of \bar{n}_g , \mathcal{Q} and \mathcal{E} in each redshift bin are given in Appendix C, Table 6. As in the case of SKAO2, we multiply the tabulated values by an amplitude factor with fiducial value 1: $\mathcal{E} \rightarrow \mathcal{E}_0 \mathcal{E}$, $\mathcal{Q} \rightarrow \mathcal{Q}_0 \mathcal{Q}$.

The three bias functions and the number densities for the two surveys are displayed in Figure 2.

In Figure 3 we show the relative contributions of the non-integrated (NI), integrated (I) and total (NI + I) corrections to the standard (S) power spectrum monopole. It is clear that the relativistic and wide-angle corrections increase in magnitude as k decreases below the equality scale k_{eq} . In addition, it is striking that in nearly all cases the non-integrated (wide-angle and local relativistic) corrections *decrease* the ultra-large scale power, while the integrated (lensing + time delay + integrated Sachs-Wolfe) corrections increase this power. As a result, the NI and I corrections partially cancel.

It is also interesting to check whether the integrated Sachs-Wolfe and time delay (ISW + TD) corrections are much smaller than the lensing (L) correction, as is typically assumed. Figure 5 shows the magnitude of the ISW + TD corrections relative to the L power spectrum monopole. It is apparent that ISW + TD is mainly much smaller than L, but there are cases where it is non-negligible – and even dominant.

It is clear from Figure 3 (S + NI + I curves) that the relativistic and wide-angle corrections become significant on the largest scales – similar to the effect of scale-dependent bias from local PNG. Figure 6 confirms this expectation, showing how a suitable choice of f_{NL} at each redshift leads to behaviour that is similar to the total correction (NI + I) in the absence of local PNG ($f_{\text{NL}} = 0$).

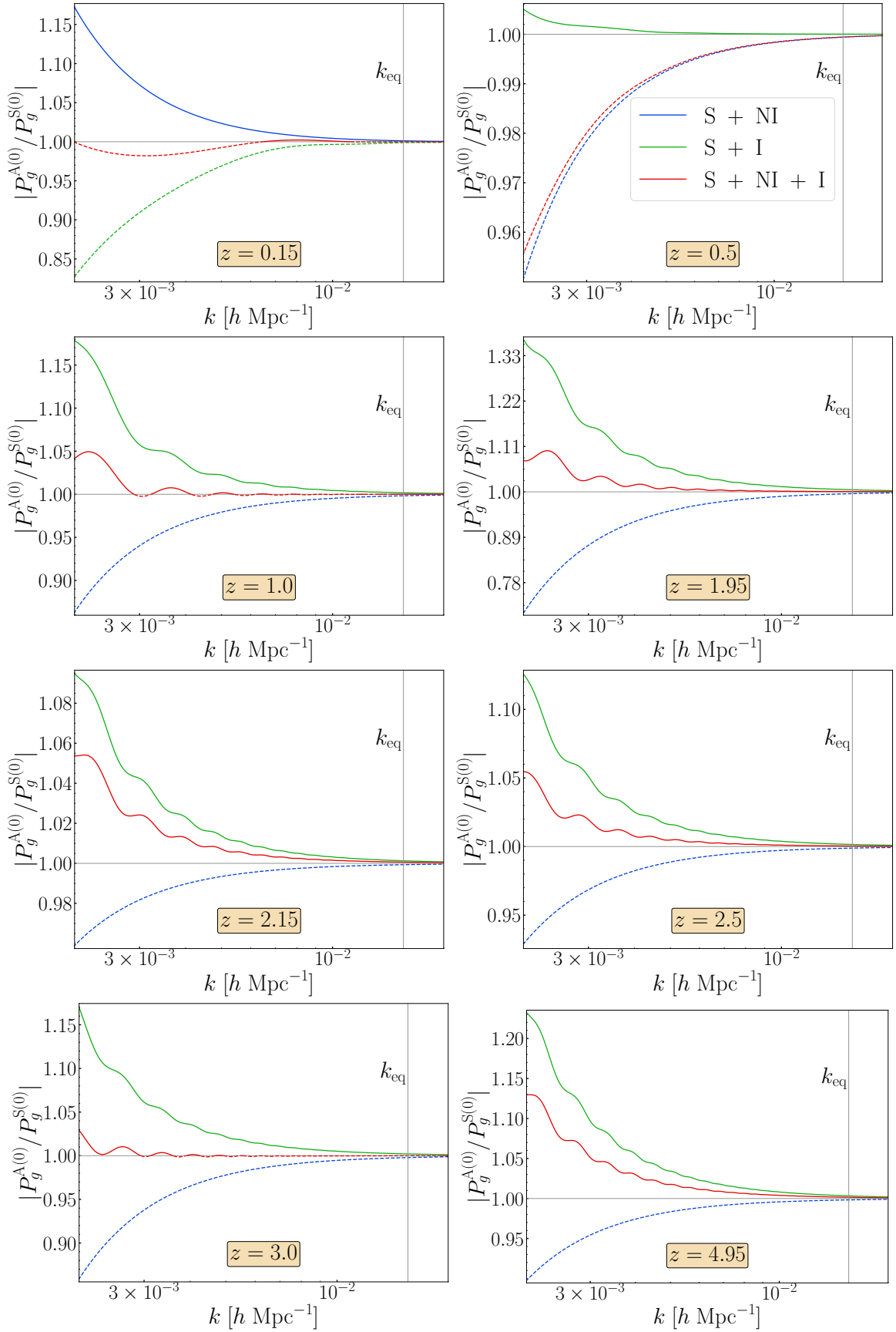


Figure 3. Relative contributions of the non-integrated (NI), integrated (I) and total (NI + I) corrections to the standard power spectrum monopole – i.e., $P_g^{A(0)}/P_g^{S(0)}$, where A = S+NI (blue), S+I (green), S+NI+I (red). These are shown for SKAO2 (*top two rows*) and MegaMapper (*bottom two rows*), at the indicated redshifts. Dashed lines indicate negative values for the corrections.

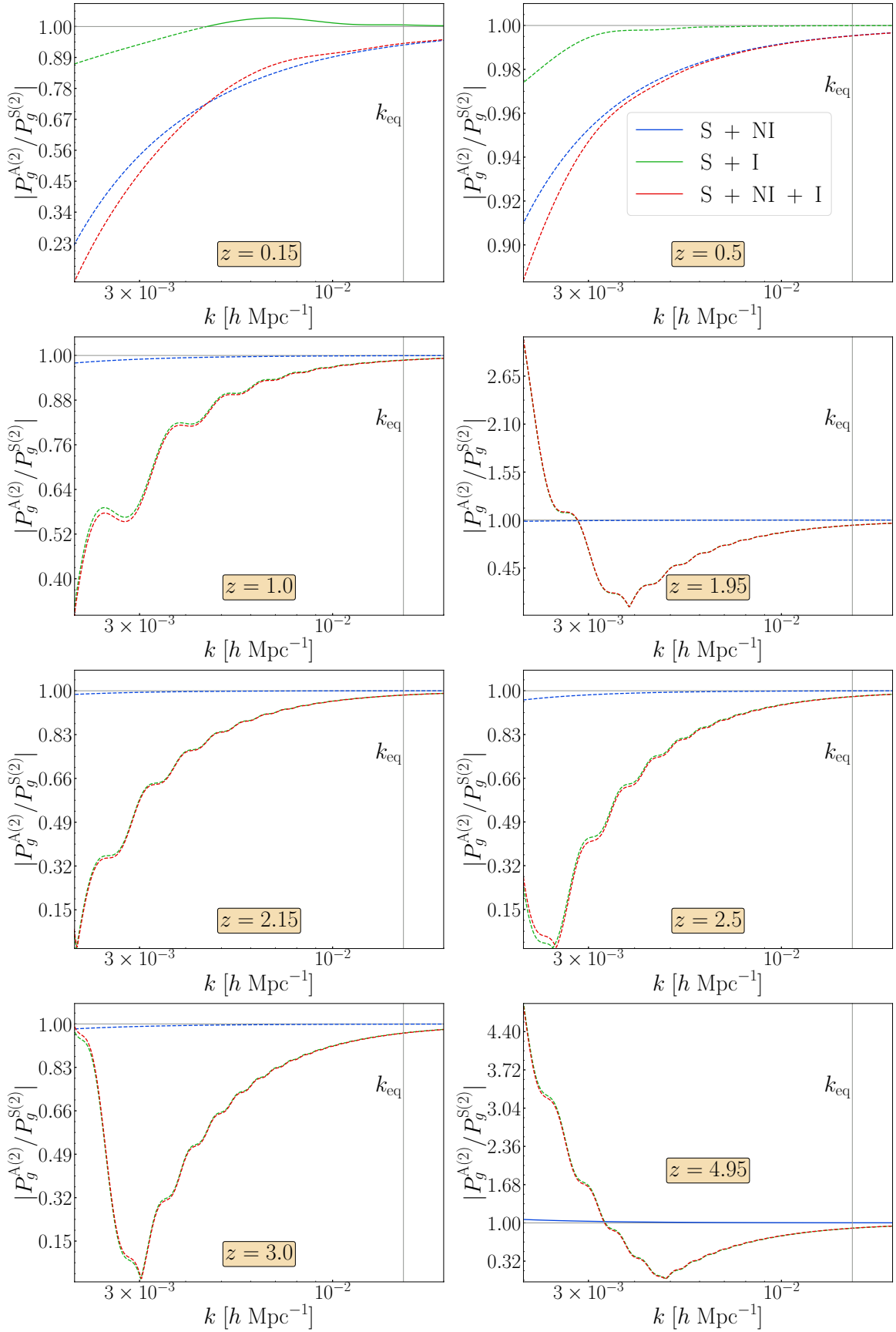


Figure 4. Same as in Figure 3, but for the relative contributions of the non-integrated (NI), integrated (I) and total (NI + I) corrections to the standard quadrupole.

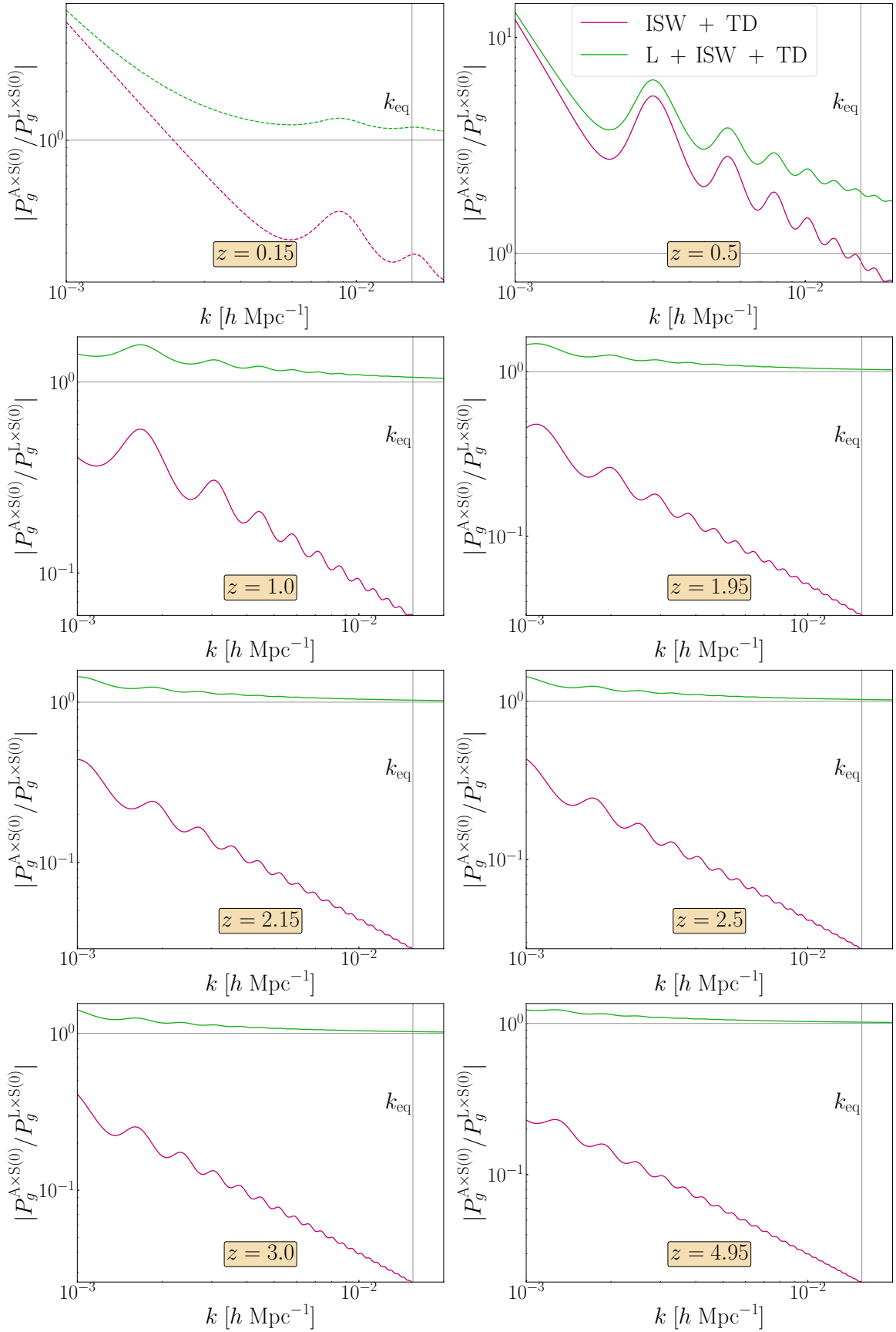


Figure 5. For the same cases as in Figure 3, but here showing the magnitude of the integrated Sachs-Wolfe + time-delay (ISW + TD) corrections relative to the lensing (L) – i.e., $P_g^{A \times S(0)} / P_g^{L \times S(0)}$, where A = ISW+TD (magenta), L+ISW+TD (green). These are shown for SKAO2 (top two rows) and MegaMapper (bottom two rows), at the indicated redshifts.

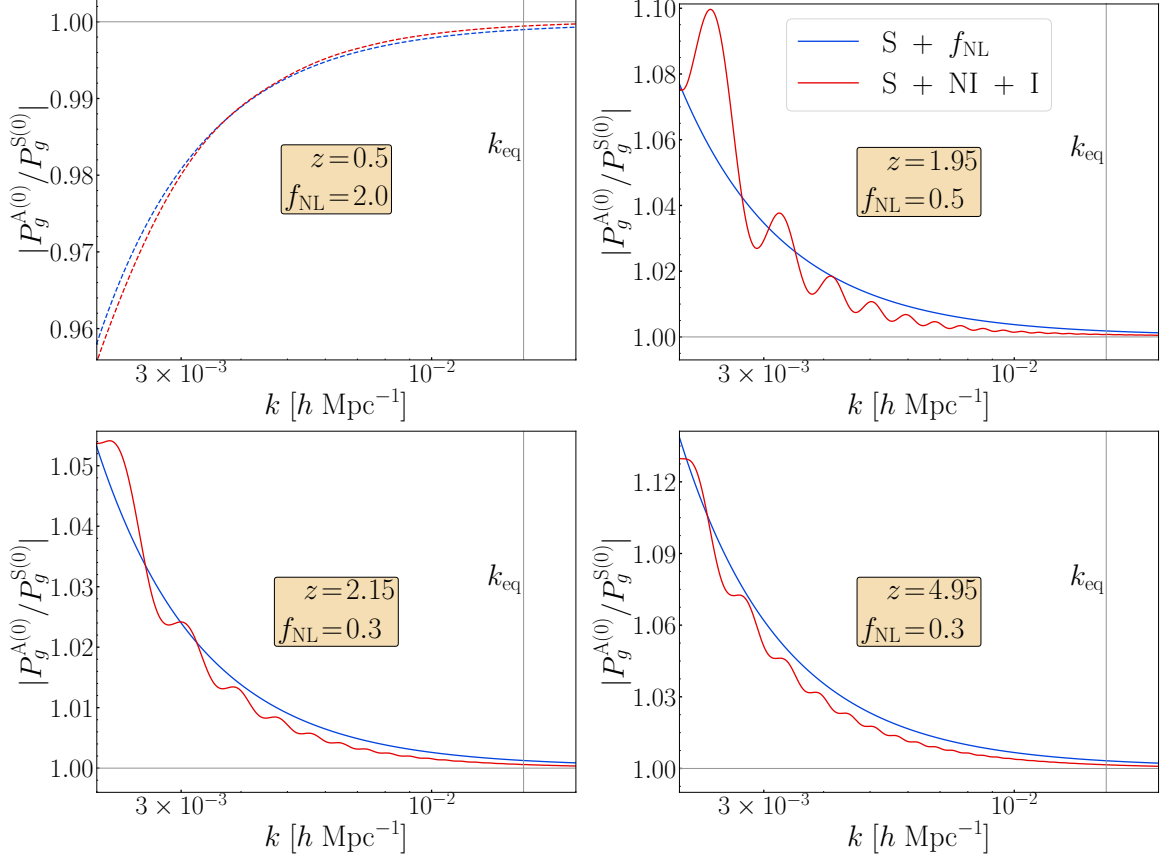


Figure 6. Comparison between relativistic + wide-angle effects and local primordial non-Gaussianity – using the ratios $P_g^{A(0)}/P_g^{S(0)}$, where $A = S + \text{NI} + \text{I}$ (red) and $S + f_{\text{NL}}$ (blue). The value of f_{NL} indicated in the plots is chosen so that $S + f_{\text{NL}}$ approximately matches $S + \text{NI} + \text{I}$. The top row shows SKAO2 and the bottom row is MegaMapper, with the redshifts shown in the panels.

3 Constraining local primordial non-Gaussianity

The covariance between the multipoles ℓ and ℓ' is [39]

$$C_{\ell\ell'}(z, k) = \frac{(2\ell + 1)(2\ell' + 1)}{2} \int_{-1}^1 d\mu \mathcal{L}_\ell(\mu)\mathcal{L}_{\ell'}(\mu)\sigma(z, k, \mu)^2, \quad (3.1)$$

where the variance per k - and μ -bin in each z -bin is

$$\sigma^2 = \frac{2}{N_k} \left[P_g + \frac{1}{\bar{n}_g} \right]^2. \quad (3.2)$$

Here

$$N_k = \frac{4\pi k^2 \Delta k}{k_f^3}, \quad k_f = \frac{2\pi}{V_s^{1/3}}, \quad V_s = \frac{\Omega_{\text{sky}}}{3} \left[r(z + \Delta z/2)^3 - r(z - \Delta z/2)^3 \right]. \quad (3.3)$$

For the binning, we choose $\Delta z = 0.1$ and $\Delta k = k_f$. In order to avoid nonlinearity, we choose a conservative maximum mode in each z -bin:

$$k_{\text{max}}(z) = 0.08 (1 + z)^{2/(2+n_s)} h \text{ Mpc}^{-1}. \quad (3.4)$$

The minimum mode, corresponding to the largest wavelength accessible in each z -bin, is determined by the longest-wavelength mode and the perturbative approximation required for the wide-angle corrections, in each redshift bin [34]:

$$k_{\text{min}}(z) = \max \left[k_f(z), \frac{1}{r(z)} \right]. \quad (3.5)$$

We use the monopole and quadrupole, neglecting the information from (and cross-correlation with) the higher multipoles. The general covariance matrix per k -bin in a z -bin is

$$\mathbf{C}(z, k) = \begin{pmatrix} C_{00}(z, k) & C_{02}(z, k) \\ C_{20}(z, k) & C_{22}(z, k) \end{pmatrix}, \quad (3.6)$$

and the Fisher matrix is

$$F_{\alpha\beta}^{\mathbf{D}}(z) = \sum_{k=k_{\text{min}}}^{k_{\text{max}}} \partial_\alpha \mathbf{D} \cdot \mathbf{C}(z, k)^{-1} \cdot \partial_\beta \mathbf{D}^{\text{T}}, \quad (3.7)$$

where \mathbf{D} is the data vector of the multipoles of the power spectrum and $\partial_\alpha = \partial/\partial\vartheta_\alpha$, with ϑ_α the parameters to be constrained. Since our focus is on the corrections to the power spectrum rather than realistic forecasts, we include only two cosmological parameters, together with f_{NL} and three nuisance parameters:

$$\vartheta_\alpha = (A_s, n_s, f_{\text{NL}}; b_0, \mathcal{E}_0, \mathcal{Q}_0). \quad (3.8)$$

The fiducial values $\bar{A}_s = 2.105 \times 10^{-9}$, $\bar{n}_s = 0.9665$ for the Λ CDM cosmological parameters are taken from Planck [40], and the remaining Λ CDM parameters are fixed at their Planck values. We take $\bar{f}_{\text{NL}} = 0$ and the nuisance fiducials are $\bar{b}_0 = 1$, $\bar{\mathcal{E}}_0 = 1$, $\bar{\mathcal{Q}}_0 = 1$.

For comparison we investigate the following four cases:

- $D = P_g^{(0)}$ and $C = C_{00}$: monopole only.
- $D = P_g^{(2)}$ and $C = C_{22}$: quadrupole only.
- $D = (P_g^{(0)}, P_g^{(2)})$ and $C_{02} = C_{20} = 0$: $P_g^{(0)} + P_g^{(2)}$ (uncorrelated).
- $D = (P_g^{(0)}, P_g^{(2)})$ and $C_{02} = C_{20} \neq 0$: $P_g^{(0)} \times P_g^{(2)}$ (correlated).

The results of the Fisher analysis, are shown in [Figure 7](#) and summarised in [Table 2](#). (See also [Appendix D](#), [Figure 10](#).)

Table 2. Marginalised 1σ errors on f_{NL}, A_s, n_s from SKAO2 and MegaMapper surveys.

Survey	Case	$\sigma(f_{\text{NL}})$	$\sigma(A_s)/\bar{A}_s$	$\sigma(n_s)/\bar{n}_s$
SKAO2	$P_g^{(0)}$	5.62	0.0251	0.00278
	$P_g^{(2)}$	57.9	0.104	0.0111
	$P_g^{(0)} + P_g^{(2)}$	3.36	0.00618	0.00244
	$P_g^{(0)} \times P_g^{(2)}$	3.05	0.00602	0.00242
MegaMapper	$P_g^{(0)}$	1.84	0.0265	0.00155
	$P_g^{(2)}$	24.1	0.178	0.0123
	$P_g^{(0)} + P_g^{(2)}$	0.711	0.00590	0.00119
	$P_g^{(0)} \times P_g^{(2)}$	0.669	0.006	0.00118
SKAO2 + MegaMapper	$P_g^{(0)} \times P_g^{(2)}$	0.578	0.00397	0.000946

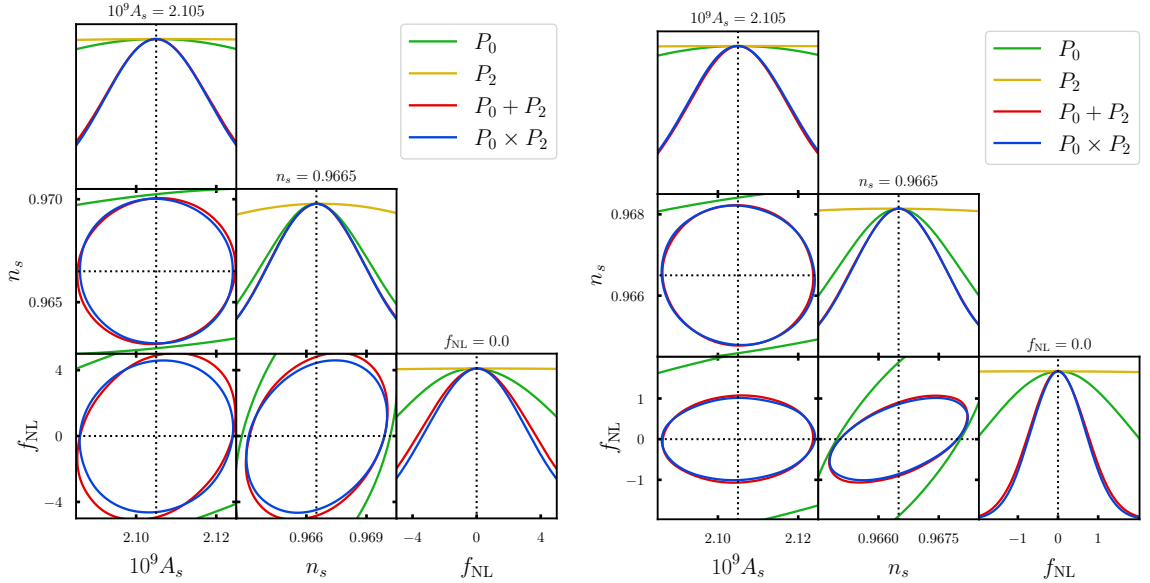


Figure 7. Contour plots of the 1σ marginal errors for different data vectors: SKAO2 HI galaxy sample (*left*) and MegaMapper LBG sample (*right*).

4 Bias on the estimate of f_{NL}

As shown in Figure 6, relativistic and wide-angle corrections can approximately mimic the effect of substantial values of f_{NL} (which change with z). We thus expect that measurements of f_{NL} when using the standard power spectrum, i.e., without relativistic + wide-angle corrections, could be biased away from the true value of f_{NL} . In order to quantify this bias, or shift, we introduce a ‘theory parameter’ ε which distinguishes between the true power spectrum ($\varepsilon = 1$) and the approximate standard power spectrum ($\varepsilon = 0$):

$$P_g = P_g^{\text{S}} + \varepsilon P_g^{\text{corr}}. \quad (4.1)$$

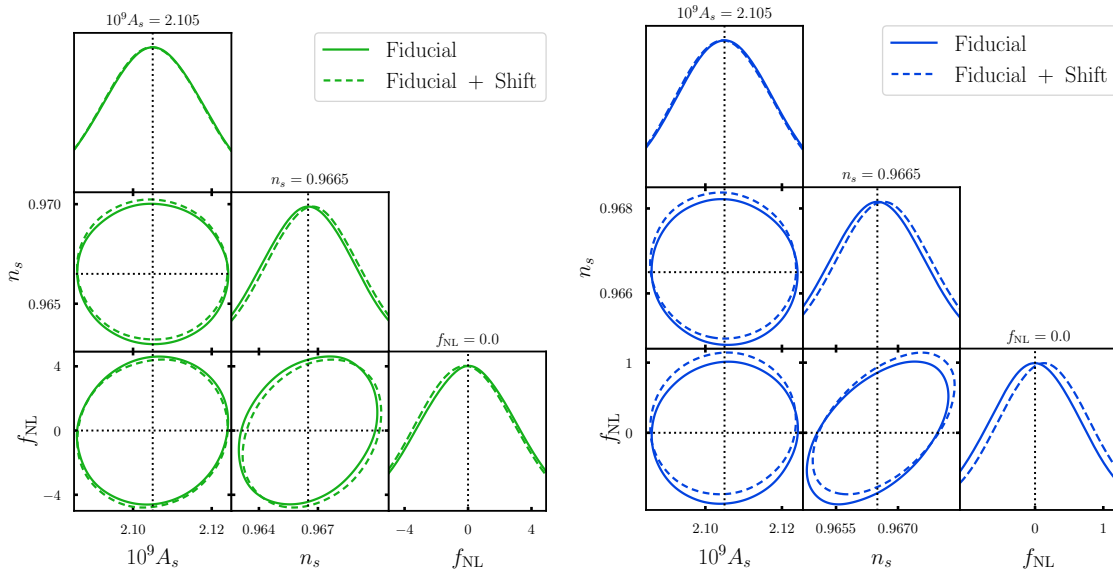


Figure 8. Contour plots showing the shifts on the parameters from $P_g^{(0)} \times P_g^{(2)}$ for the SKAO2 HI galaxy (left) and MegaMapper LBG (right) samples.

Since the true and incorrect models are competing and nested models, they have the same number 6 of common parameters and the correct model has 1 extra parameter. The value of f_{NL} in the incorrect model shifts to compensate for the fact that ε is being kept fixed at the incorrect fiducial value $\varepsilon = 0$. Within a Gaussian Fisher formalism, the bias on the value of f_{NL} may be computed as (see e.g. [41] and references therein)

$$\delta f_{\text{NL}} = f_{\text{NL}}^{\text{true}} - f_{\text{NL}}^{\text{wrong}} = -(\overset{0}{\mathbf{F}}^{-1})_{f_{\text{NL}}\alpha} \overset{1}{\mathbf{F}}_{\alpha\varepsilon} \delta\varepsilon. \quad (4.2)$$

Here there is a sum over α , i.e. over the parameters in $\overset{0}{\mathbf{F}}$, which is the Fisher matrix in the incorrect model ($\varepsilon = 0$). The Fisher matrix in the true model, $\overset{1}{\mathbf{F}}$, has one extra row and column due to the extra parameter ε . By definition of ε , its shift is $\delta\varepsilon = \varepsilon^{\text{true}} - \varepsilon^{\text{wrong}} = 1$.

The results of the shift $\delta(\vartheta_i)$ in the value of $\vartheta_i = (f_{\text{NL}}, A_s, n_s)$ are presented in Table 3–Table 5. Since the shift must be compared with the precision of measurement, we give the normalised shift $\delta(\vartheta_i)/\sigma(\vartheta_i)$. Note that $\sigma(\vartheta_i)$ is the marginalised error from the correct model.

Table 3. Normalised shift, $\delta(f_{\text{NL}})/\sigma(f_{\text{NL}})$, on the value of f_{NL} for the case $P_g^{(0)} \times P_g^{(2)}$ from galaxy surveys SKAO2 and MegaMapper with different P_g^{corr} .

Surveys	NI	I	NI + I
SKAO2	0.458	-0.502	-0.0736
MegaMapper	0.282	-0.275	0.206
SKAO2 + MegaMapper	0.634	-0.335	0.200

Table 4. Normalised shift, $\delta(A_s)/\sigma(A_s)$, on the value of A_s for the case $P_g^{(0)} \times P_g^{(2)}$ from galaxy surveys SKAO2 and MegaMapper with different P_g^{corr} .

Survey	NI	I	NI + I
SKAO2	-0.209	0.0484	-0.0765
MegaMapper	-0.241	0.0320	-0.190
SKAO2 + MegaMapper	-0.272	-0.0824	-0.225

Table 5. Normalised shift, $\delta(n_s)/\sigma(n_s)$, on the value of n_s for the case $P_g^{(0)} \times P_g^{(2)}$ from galaxy surveys SKAO2 and MegaMapper with different P_g^{corr} .

Surveys	NI	I	NI + I
SKAO2	-0.00655	0.133	0.0915
MegaMapper	0.155	0.0579	0.140
SKAO2 + MegaMapper	-0.0115	0.223	0.162

5 Conclusion

In this work, we investigate the impact of the local and integrated corrections on the galaxy power spectrum and their implications for constraining the local primordial non-Gaussianity parameter, f_{NL} . Relativistic and wide-angle corrections significantly influence the monopole (see Figure 3) and especially the quadrupole (Figure 4) of the power spectrum at scales $k < k_{\text{eq}}$. Non-integrated corrections, such as wide-angle and Doppler terms, and integrated corrections, including lensing, exhibit opposing behaviours for the surveys considered, leading to a partial cancellation of their contributions. While integrated Sachs-Wolfe and time-delay effects are generally smaller than lensing corrections, they can be comparable at certain redshifts and scales (Figure 5) and thus we include them for accurate modeling of large-scale galaxy clustering.

Our results demonstrate that incorporating the quadrupole provides significant gains in the precision of f_{NL} constraints. For SKAO2, the marginalised error on f_{NL} is reduced from $\sigma(f_{\text{NL}}) = 5.62$ when only the monopole is used to $\sigma(f_{\text{NL}}) = 3.05$ when the monopole and quadrupole are combined, an improvement of $\sim 46\%$. MegaMapper achieves tighter constraints due to its higher redshift coverage, with $\sigma(f_{\text{NL}}) = 0.669$ for the combined monopole and quadrupole analysis, an improvement of $\sim 64\%$ compared to the monopole-only case. This reflects the quadrupole’s sensitivity to relativistic and wide-angle corrections

When SKAO2 and MegaMapper data are jointly analysed, the error on f_{NL} is further reduced to $\sigma(f_{\text{NL}}) = 0.578$, demonstrating the power of combining low- and high-redshift data in constraining primordial non-Gaussianity.

Relativistic and wide-angle corrections also affect the estimation of f_{NL} , as these effects can partly mimic the scale-dependent bias introduced by primordial non-Gaussianity. If these corrections are neglected, non-negligible biases are introduced in f_{NL} estimates [7–11]. (Note that the effect of lensing is stronger in photometric than in spectroscopic surveys [7, 42, 43].) For SKAO2, the shift in f_{NL} due to non-integrated corrections alone is 0.46σ , while for MegaMapper it is 0.28σ . When both integrated and non-integrated corrections are included, the shifts are reduced, but remain non-trivial. The shifts due to integrated and non-integrated corrections partly cancel, especially for SKAO2, resulting in relatively small biases of approximately 0.1σ to 0.2σ . The combined SKAO2 and MegaMapper analysis shows a shift of 0.2σ in f_{NL} if these corrections are ignored, emphasising the necessity of incorporating them in future analyses.

Compared to previous studies, such as [9] for SKAO2 and [11] for Euclid-like spectroscopic surveys, the shifts we find in f_{NL} are smaller. This difference arises from the methodologies; these earlier works employed angular power spectrum analyses, which naturally include all relativistic and wide-angle effects without approximation, as well as cross-bin correlations. In contrast, our Fourier-space analysis neglects such correlations, which likely contributes to the smaller biases observed here. Furthermore, our lensing treatment follows the approximation introduced by [32], which omits several potentially important contributions:

- The lensing-lensing correlation, which is not suppressed by any positive power of k/\mathcal{H} , is neglected.
- In particular, the off-diagonal lensing-lensing correlations are largest for the most widely separated redshift bins [11], and these are neglected.
- Indeed, there are no cross-bin correlations of any type in a standard Fourier analysis (see [44] for a discussion).

We intend to address some of these limitations in a follow-up investigation.

Acknowledgements: SG and RM are supported by the South African Radio Astronomy Observatory and the National Research Foundation (grant no. 75415). SJ is supported by the Stellenbosch University Astrophysics Research Group fund. We thank Stefano Camera and Chris Clarkson for useful discussions.

A Multipoles of the non-integrated power spectrum

The monopoles of the standard power spectrum and the non-integrated correction from [34] (in the midpoint case, i.e, $t = 1/2$) are:

$$\begin{aligned}
\frac{P_g^{\text{S}(0)}}{P} &= (b + b_{\text{ng}})^2 + \frac{2}{3}(b + b_{\text{ng}})f + \frac{1}{5}f^2 \tag{A.1} \\
\frac{P_g^{\text{NI}(0)}}{P} &= \frac{1}{3} \frac{1}{k^2} [(\gamma^{\text{D}})^2 + 2(f + 3b + 3b_{\text{ng}})\gamma^{\Phi}] \\
&\quad + \frac{2}{15} \frac{f}{kr} \left[-\frac{2}{k}\gamma^{\text{D}} + \frac{\mathcal{H}}{k} \left(\mathcal{E} - 2\mathcal{Q} - \frac{\mathcal{H}'}{\mathcal{H}^2} \right) (f + 5b + 5b_{\text{ng}} + 5k \partial_k b_{\text{ng}}) \right] \\
&\quad + \frac{2}{15} \frac{f}{(kr)^2} \left[\frac{11}{14}f + (1 - \mathcal{Q})[f - 5b - 5b_{\text{ng}} - 5k \partial_k b_{\text{ng}}] \right. \\
&\quad \quad \quad \left. - \frac{1}{2}(3b + 3b_{\text{ng}} + 5k \partial_k b_{\text{ng}} + k^2 \partial_k^2 b_{\text{ng}}) \right] \\
&\quad + \frac{2}{15} f \left\{ \frac{1}{kr} \left[-\frac{2}{k}\gamma^{\text{D}} + \frac{\mathcal{H}}{k} \left(\mathcal{E} - 2\mathcal{Q} - \frac{\mathcal{H}'}{\mathcal{H}^2} \right) (f + 5b + 5b_{\text{ng}}) \right] \right. \\
&\quad \quad \quad \left. + \frac{1}{(kr)^2} \left[\frac{37}{14}f + (1 - \mathcal{Q})(f - 5b - 5b_{\text{ng}}) \right. \right. \\
&\quad \quad \quad \left. \left. - \frac{1}{2}(5b + 5b_{\text{ng}} + 2k \partial_k b_{\text{ng}}) \right] \right\} \frac{k \partial_k P}{P} \\
&\quad + \frac{1}{15} \frac{f}{(kr)^2} \left\{ \frac{13}{7}f - \left[b + b_{\text{ng}} + \frac{1}{k^2}\gamma^{\Phi} - \frac{3}{2} \frac{\mathcal{H}}{k} \left(\mathcal{E} - 2\mathcal{Q} - \frac{\mathcal{H}'}{\mathcal{H}^2} \right) \frac{1}{k}\gamma^{\text{D}} \right] \right. \\
&\quad \quad \quad \left. + f \frac{\mathcal{H}^2}{k^2} \left(\mathcal{E} - 2\mathcal{Q} - \frac{\mathcal{H}'}{\mathcal{H}^2} \right)^2 \right\} \frac{k^2 \partial_k^2 P}{P}. \tag{A.2}
\end{aligned}$$

The quadrupoles are

$$\begin{aligned}
\frac{P_g^{\text{S}(2)}}{P} &= \frac{4}{3}(b + b_{\text{ng}})f + \frac{4}{7}f^2 \tag{A.3} \\
\frac{P_g^{\text{NI}(2)}}{P} &= \frac{2}{3} \frac{1}{k^2} [(\gamma^{\text{D}})^2 + 2f \gamma^{\Phi}] \\
&\quad + \frac{2}{21} \frac{f}{kr} \left[\frac{\mathcal{H}}{k} \left(\mathcal{E} - 2\mathcal{Q} - \frac{\mathcal{H}'}{\mathcal{H}^2} \right) (10f + 14b + 14b_{\text{ng}} - 7k \partial_k b_{\text{ng}}) - \frac{20}{k}\gamma^{\text{D}} \right]
\end{aligned}$$

$$\begin{aligned}
& -\frac{2}{21} \frac{f}{(kr)^2} \left[-f + 2(1 - \mathcal{Q}) (13f + 28b + 28b_{\text{ng}} - 14k \partial_k b_{\text{ng}}) \right. \\
& \quad \left. + \frac{11}{2} (6b + 6b_{\text{ng}} - 2k \partial_k b_{\text{ng}} - k^2 \partial_k^2 b_{\text{ng}}) \right] \\
& + \frac{2}{21} f \left\{ \frac{1}{kr} \left[\frac{\mathcal{H}}{k} \left(\varepsilon - 2\mathcal{Q} - \frac{\mathcal{H}'}{\mathcal{H}^2} \right) (f - 7b - 7b_{\text{ng}}) - \frac{2}{k} \gamma^{\text{D}} \right] \right. \\
& \quad \left. + \frac{1}{(kr)^2} \left[2(1 - \mathcal{Q})(5f + 14b + 14b_{\text{ng}}) \right. \right. \\
& \quad \quad \left. \left. + 11(f + b + b_{\text{ng}} + k \partial_k b_{\text{ng}}) \right] \right\} \frac{k \partial_k P}{P} \\
& + \frac{1}{21} \frac{f}{(kr)^2} \left\{ 3f + 11(b + b_{\text{ng}} + \frac{1}{k^2} \gamma^{\Phi}) + \frac{3\mathcal{H}}{2k} \left(\varepsilon - 2\mathcal{Q} - \frac{\mathcal{H}'}{\mathcal{H}^2} \right) \frac{1}{k} \gamma^{\text{D}} \right. \\
& \quad \left. - 4f \frac{\mathcal{H}^2}{k^2} \left(\varepsilon - 2\mathcal{Q} - \frac{\mathcal{H}'}{\mathcal{H}^2} \right)^2 \right\} \frac{k^2 \partial_k^2 P}{P}. \tag{A.4}
\end{aligned}$$

where

$$\gamma^{\text{D}} = \mathcal{H}f \left[\varepsilon - 2\mathcal{Q} + \frac{2(\mathcal{Q} - 1)}{r\mathcal{H}} - \frac{\mathcal{H}'}{\mathcal{H}^2} \right], \tag{A.5}$$

$$\gamma^{\Phi} = \frac{3}{2} \Omega_m \mathcal{H}^2 \left[2 + \varepsilon - f - 4\mathcal{Q} + \frac{2(\mathcal{Q} - 1)}{r\mathcal{H}} - \frac{\mathcal{H}'}{\mathcal{H}^2} \right] + \mathcal{H}^2 f (3 - \varepsilon). \tag{A.6}$$

The derivatives of P are shown in [Figure 9](#).

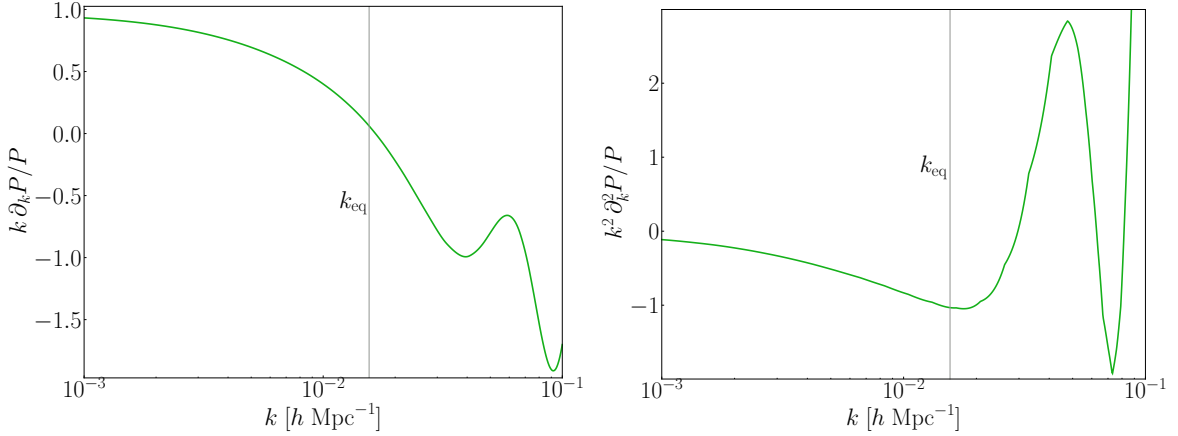


Figure 9. Derivatives of the linear matter power spectrum P .

B Derivation of the integrated correction to the power spectrum

Here we show how to derive the equations in [section 2](#) and thus recover the results of [\[32\]](#). The standard (S) contribution to the number count density contrast is the galaxy density contrast and linear Kaiser redshift-space distortions. It is given by

$$\Delta_g^S(\mathbf{x}_a) = \int \frac{d^3 \mathbf{k}_a}{(2\pi)^3} \exp(i \mathbf{k}_a \cdot \mathbf{x}_a) \mathcal{K}^S(x_a, k_a, \mu_a) D(x_a) \delta_0(\mathbf{k}_a), \quad (\text{B.1})$$

where δ_0 is the matter density contrast at $z = 0$ and the standard Fourier kernel is given by [Equation 1.4](#). The integrated (I) relativistic correction to [\(B.1\)](#) is

$$\Delta_g^{\text{int}}(\mathbf{x}_a) = \int \frac{d^3 \mathbf{k}_a}{(2\pi)^3} \int_0^{x_a} d\tilde{r} \exp(i \mathbf{k}_a \cdot \tilde{\mathbf{r}}) \mathcal{K}^{\text{int}}(x_a, \tilde{r}, k_a, \mu_a) D(\tilde{r}) \delta_0(\mathbf{k}_a), \quad (\text{B.2})$$

where \mathcal{K}^{int} is given by [Equation 2.1](#). Then the cross-correlation between Δ_g^S and Δ_g^{int} is given by

$$\begin{aligned} \langle \Delta_g^S(\mathbf{x}_1) \Delta_g^{\text{int}}(\mathbf{x}_2) \rangle &= \int \frac{d^3 \mathbf{k}_1}{(2\pi)^3} \int \frac{d^3 \mathbf{k}_2}{(2\pi)^3} \int_0^{x_2} d\tilde{r} \exp\left\{i \left[\mathbf{k}_1 \cdot \mathbf{x}_1 + \left(\frac{\tilde{r}}{x_2}\right) \mathbf{k}_2 \cdot \mathbf{x}_2 \right]\right\} \\ &\times \mathcal{K}^S(x_1, k_1, \mu_1) \mathcal{K}^{\text{int}}(x_2, \tilde{r}, k_2, \mu_2) D(x_1) D(\tilde{r}) \langle \delta_0(\mathbf{k}_1) \delta_0(\mathbf{k}_2) \rangle. \end{aligned} \quad (\text{B.3})$$

Here we make the plane-parallel approximation [Equation 1.5](#), so that $\hat{\tilde{\mathbf{r}}} \approx \hat{\mathbf{x}}_1 \approx \hat{\mathbf{x}}_2$. Thus we neglect mixing with wide-angle corrections, following [\[32\]](#). For the mid-point configuration ([Figure 1](#)), $\mathbf{x}_1 = \mathbf{r} - \mathbf{x}/2$ and $\mathbf{x}_2 = \mathbf{r} + \mathbf{x}/2$. Using $\langle \delta_0(\mathbf{k}_1) \delta_0(\mathbf{k}_2) \rangle = (2\pi)^3 P_0(k_1) \delta^D(\mathbf{k}_1 + \mathbf{k}_2)$ and integrating over \mathbf{k}_2 , [Equation B.3](#) becomes

$$\begin{aligned} \langle \Delta_g^S(\mathbf{x}_1) \Delta_g^{\text{int}}(\mathbf{x}_2) \rangle &= \int \frac{d\mathbf{k}_1}{(2\pi)^3} \int_0^{x_2} d^3 \tilde{r} \exp\left\{i \left[\left(\frac{x_2 - \tilde{r}}{x_2}\right) \mathbf{k}_1 \cdot \mathbf{r} - \left(\frac{x_2 + \tilde{r}}{2x_2}\right) \mathbf{k}_1 \cdot \mathbf{x} \right]\right\} \\ &\times \mathcal{K}^S(x_1, k_1, \mu_1) \mathcal{K}^{\text{int}*}(x_2, \tilde{r}, k_1, \mu_1) D(x_1) D(\tilde{r}) P_0(k_1). \end{aligned} \quad (\text{B.4})$$

At leading order, $x_1 = x_2 = r$ (neglecting mixing with wide-angle corrections) and then [Equation B.4](#) becomes

$$\begin{aligned} \langle \Delta_g^S(\mathbf{r} - \mathbf{x}/2) \Delta_g^{\text{int}}(\mathbf{r} + \mathbf{x}/2) \rangle &= \int \frac{d^3 \mathbf{k}_1}{(2\pi)^3} \int_0^r d\tilde{r} \exp\left\{i \left[\left(\frac{r - \tilde{r}}{r}\right) \mathbf{k}_1 \cdot \mathbf{r} - \left(\frac{r + \tilde{r}}{2r}\right) \mathbf{k}_1 \cdot \mathbf{x} \right]\right\} \\ &\times \mathcal{K}^S(r, k_1, \mu_1) \mathcal{K}^{\text{int}*}(r, \tilde{r}, k_1, \mu_1) D(x_1) D(\tilde{r}) P_0(k_1). \end{aligned} \quad (\text{B.5})$$

The Fourier transform of [Equation B.5](#) gives the cross-power spectrum:

$$\begin{aligned} P_g^{\text{S} \times \text{int}}(\mathbf{r}, \mathbf{k}) &= \int d^3 \mathbf{x} \exp(-i \mathbf{k} \cdot \mathbf{x}) \langle \Delta_g^S(\mathbf{r} - \mathbf{x}/2) \Delta_g^{\text{int}}(\mathbf{r} + \mathbf{x}/2) \rangle \\ &= \int_0^r d\tilde{r} \int d^3 \mathbf{k}_1 \delta^D \left[\mathbf{k} + \left(\frac{r + \tilde{r}}{2r}\right) \mathbf{k}_1 \right] \exp \left[i \left(\frac{r - \tilde{r}}{r}\right) \mathbf{k}_1 \cdot \mathbf{r} \right] \\ &\times \mathcal{K}^S(r, k_1, \mu_1) \mathcal{K}^{\text{int}*}(r, \tilde{r}, k_1, \mu_1) D(r) D(\tilde{r}) P_0(k_1). \end{aligned} \quad (\text{B.6})$$

The Dirac-delta function can be simplified:

$$\delta^D[\mathbf{k}_1 + G(r, \tilde{r}) \mathbf{k}] = G(r, \tilde{r})^{-3} \delta^D[\mathbf{k}_1 + G(r, \tilde{r})^{-1} \mathbf{k}], \quad (\text{B.7})$$

where we used [Equation 2.6](#). Then [\(B.6\)](#) becomes

$$\begin{aligned} P_g^{\text{S}\times\text{int}}(r, k, \mu) &= \int_0^r d\tilde{r} G(r, \tilde{r})^{-3} \exp[-i\mu G(r, \tilde{r})^{-1} k (r - \tilde{r})] \\ &\quad \times \mathcal{K}^{\text{S}}(r, k, \mu) \mathcal{K}^{\text{int}*}(r, \tilde{r}, k, \mu) D(r) D(\tilde{r}) P_0(k/G(r, \tilde{r})) \\ &\equiv \int_0^r d\tilde{r} \mathcal{J}(r, \tilde{r}, k, \mu). \end{aligned} \quad (\text{B.8})$$

The total cross-power spectrum for the integrated relativistic effects at leading order is

$$P_g^{\text{I}}(r, k, \mu) = P_g^{\text{S}\times\text{int}}(r, k, \mu) + P_g^{\text{int}\times\text{S}}(r, k, \mu) = \int_0^r d\tilde{r} [\mathcal{J}(r, \tilde{r}, k, \mu) + \mathcal{J}^*(r, \tilde{r}, k, \mu)]. \quad (\text{B.9})$$

Multipoles of the integrated power spectrum

Gauss-Legendre quadrature is an efficient method for numerically approximating definite integrals by transforming the integration interval into a standard domain. For a 2D numerical integration over a rectangular domain $[x_{\min}, x_{\max}] \times [y_{\min}, y_{\max}]$, the integral

$$F = \int_{x_{\min}}^{x_{\max}} \int_{y_{\min}}^{y_{\max}} dx dy f(x, y), \quad (\text{B.10})$$

must first be transformed into the reference interval $[-1, 1] \times [-1, 1]$ before applying the Gauss-Legendre quadrature rule:

$$x = \frac{x_{\max} - x_{\min}}{2} \xi + \frac{x_{\max} + x_{\min}}{2}, \quad y = \frac{y_{\max} - y_{\min}}{2} \eta + \frac{y_{\max} + y_{\min}}{2}, \quad (\text{B.11})$$

where ξ and η are the new variables of integration in the interval $[-1, 1]$. The integral [Equation B.10](#) becomes:

$$F = A \int_{-1}^1 \int_{-1}^1 d\xi d\eta f\left(\frac{x_{\max} - x_{\min}}{2} \xi + \frac{x_{\max} + x_{\min}}{2}, \frac{y_{\max} - y_{\min}}{2} \eta + \frac{y_{\max} + y_{\min}}{2}\right), \quad (\text{B.12})$$

where $A = (x_{\max} - x_{\min})(y_{\max} - y_{\min})/4$. Using Gauss-Legendre quadrature, the integral is approximated by a weighted sum over the quadrature points:

$$F \approx A \sum_{i=1}^n \sum_{j=1}^n w_i w_j f\left(\frac{x_{\max} - x_{\min}}{2} \xi_i + \frac{x_{\max} + x_{\min}}{2}, \frac{y_{\max} - y_{\min}}{2} \eta_j + \frac{y_{\max} + y_{\min}}{2}\right), \quad (\text{B.13})$$

where ξ_i and η_j are the Gauss-Legendre quadrature points on $[-1, 1]$, and w_i, w_j are the corresponding weights.

The integrated contribution [Equation 2.9](#) is of the form:

$$P_g^{\text{I}} = \int_0^r d\tilde{r} \mathcal{I}(\tilde{r}, \mu), \quad (\text{B.14})$$

and its multipoles can be written as:

$$P_g^{\text{I}(\ell)} = \frac{2\ell + 1}{2} \int_{-1}^1 \int_0^r d\tilde{r} d\mu \mathcal{L}_\ell(\mu) \mathcal{I}(\tilde{r}, \mu) \approx \frac{2\ell + 1}{2} \frac{r}{2} \sum_{i=1}^n \sum_{j=1}^n w_i w_j \mathcal{L}_\ell(\xi_i) \mathcal{I}\left(\frac{r}{2} \eta_j + \frac{r}{2}, \xi_i\right). \quad (\text{B.15})$$

C MegaMapper functions

Table 6. MegaMapper LBG: number density, evolution bias and magnification bias (from [45]).

z	\bar{n}_g ($10^{-3} h^3 \text{Mpc}^{-3}$)	\mathcal{E}	\mathcal{Q}
2.1	2.26	2.99	1.92
2.2	1.79	3.61	1.97
2.3	1.41	3.78	2.02
2.4	1.12	3.37	2.08
2.5	0.91	2.41	2.14
2.6	0.76	1.12	2.21
2.7	0.66	-0.13	2.28
2.8	0.60	-1.04	2.36
2.9	0.55	-1.50	2.45
3.0	0.50	-1.56	2.55
3.1	0.46	-1.34	2.65
3.2	0.41	-0.99	2.76
3.3	0.37	-0.61	2.88
3.4	0.33	-0.31	3.00
3.5	0.29	-0.14	3.12
3.6	0.25	-0.16	3.24
3.7	0.22	-0.39	3.36
3.8	0.19	-0.81	3.46
3.9	0.17	-1.34	3.54
4.0	0.15	-1.82	3.61
4.1	0.14	-2.17	3.65
4.2	0.12	-2.32	3.68
4.3	0.11	-2.20	3.70
4.4	0.10	-1.78	3.71
4.5	0.09	-0.98	3.71
4.6	0.08	-0.24	3.71
4.7	0.07	1.97	3.70
4.8	0.06	4.29	3.70
4.9	0.05	7.37	3.71
5.0	0.03	11.40	3.72

D Additional contour plots

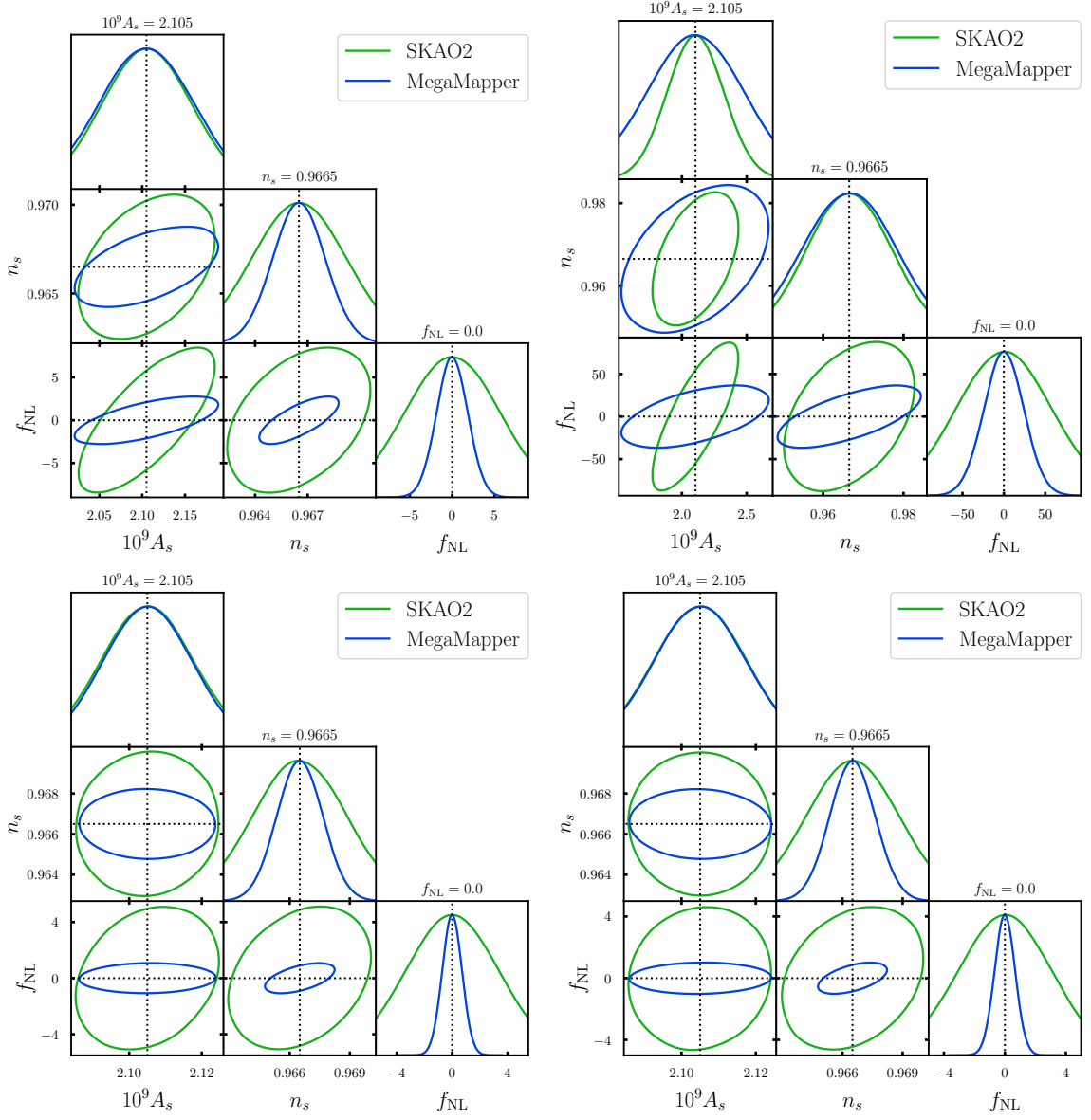


Figure 10. Contour plots of the 1σ marginal errors from SKAO2 HI galaxy and MegaMapper LBG surveys, for the cases: $P_g^{(0)}$ (top left), $P_g^{(2)}$ (top right), $P_g^{(0)} + P_g^{(2)}$ (bottom left), and $P_g^{(0)} \times P_g^{(2)}$ (bottom right).

References

- [1] N. Dalal, O. Dore, D. Huterer, and A. Shirokov, *The imprints of primordial non-gaussianities on large-scale structure: scale dependent bias and abundance of virialized objects*, *Phys. Rev. D* **77** (2008) 123514, [[arXiv:0710.4560](#)].
- [2] E. Komatsu, *Hunting for Primordial Non-Gaussianity in the Cosmic Microwave Background*, *Class. Quant. Grav.* **27** (2010) 124010, [[arXiv:1003.6097](#)].
- [3] X. Chen, *Primordial Non-Gaussianities from Inflation Models*, *Adv. Astron.* **2010** (2010) 638979, [[arXiv:1002.1416](#)].
- [4] A. Challinor and A. Lewis, *The linear power spectrum of observed source number counts*, *Phys. Rev. D* **84** (2011) 043516, [[arXiv:1105.5292](#)].
- [5] A. Raccanelli, F. Montanari, D. Bertacca, O. Doré, and R. Durrer, *Cosmological Measurements with General Relativistic Galaxy Correlations*, *JCAP* **05** (2016) 009, [[arXiv:1505.06179](#)].
- [6] D. Alonso, P. Bull, P. G. Ferreira, R. Maartens, and M. Santos, *Ultra large-scale cosmology in next-generation experiments with single tracers*, *Astrophys. J.* **814** (2015), no. 2 145, [[arXiv:1505.07596](#)].
- [7] T. Namikawa, T. Okamura, and A. Taruya, *Magnification effect on the detection of primordial non-Gaussianity from photometric surveys*, *Phys. Rev. D* **83** (2011) 123514, [[arXiv:1103.1118](#)].
- [8] M. Bruni, R. Crittenden, K. Koyama, R. Maartens, C. Pitrou, and D. Wands, *Disentangling non-Gaussianity, bias and GR effects in the galaxy distribution*, *Phys. Rev. D* **85** (2012) 041301, [[arXiv:1106.3999](#)].
- [9] S. Camera, R. Maartens, and M. G. Santos, *Einstein’s legacy in galaxy surveys*, *Mon. Not. Roy. Astron. Soc.* **451** (2015), no. 1 L80–L84, [[arXiv:1412.4781](#)].
- [10] C. S. Lorenz, D. Alonso, and P. G. Ferreira, *Impact of relativistic effects on cosmological parameter estimation*, *Phys. Rev. D* **97** (2018), no. 2 023537, [[arXiv:1710.02477](#)].
- [11] J.-A. Viljoen, J. Fonseca, and R. Maartens, *Multi-wavelength spectroscopic probes: biases from neglecting light-cone effects*, *JCAP* **12** (2021), no. 12 004, [[arXiv:2108.05746](#)].
- [12] R. Maartens, J. Fonseca, S. Camera, S. Jolicœur, J.-A. Viljoen, and C. Clarkson, *Magnification and evolution biases in large-scale structure surveys*, *JCAP* **12** (2021), no. 12 009, [[arXiv:2107.13401](#)].
- [13] N. Sailer, E. Castorina, S. Ferraro, and M. White, *Cosmology at high redshift — a probe of fundamental physics*, *JCAP* **12** (2021), no. 12 049, [[arXiv:2106.09713](#)].
- [14] **Planck** Collaboration, Y. Akrami et al., *Planck 2018 results. IX. Constraints on primordial non-Gaussianity*, *Astron. Astrophys.* **641** (2020) A9, [[arXiv:1905.05697](#)].
- [15] A. Barreira, *Can we actually constrain f_{NL} using the scale-dependent bias effect? An illustration of the impact of galaxy bias uncertainties using the BOSS DR12 galaxy power spectrum*, *JCAP* **11** (2022) 013, [[arXiv:2205.05673](#)].
- [16] A. Barreira and E. Krause, *Towards optimal and robust f_{nl} constraints with multi-tracer analyses*, *JCAP* **10** (2023) 044, [[arXiv:2302.09066](#)].
- [17] E. Fondi, L. Verde, F. Villaescusa-Navarro, M. Baldi, W. R. Coulton, G. Jung, D. Karagiannis, M. Liguori, A. Ravenni, and B. D. Wandelt, *Taming assembly bias for primordial non-Gaussianity*, *JCAP* **02** (2024) 048, [[arXiv:2311.10088](#)].
- [18] A. G. Adame, S. Avila, V. Gonzalez-Perez, G. Yepes, M. Pellejero, M. S. Wang, C.-H. Chuang, Y. Feng, J. Garcia-Bellido, and A. Knebe, *PNG-UNITsims: Halo clustering response to primordial non-Gaussianities as a function of mass*, *Astron. Astrophys.* **689** (2024) A69, [[arXiv:2312.12405](#)].

- [19] T. Matsubara, *The Correlation function in redshift space: General formula with wide angle effects and cosmological distortions*, *Astrophys. J.* **535** (2000) 1, [[astro-ph/9908056](#)].
- [20] T. Matsubara, *The gravitational lensing in redshift-space correlation functions of galaxies and quasars*, *Astrophys. J. Lett.* **537** (2000) L77, [[astro-ph/0004392](#)].
- [21] D. Bertacca, R. Maartens, A. Raccanelli, and C. Clarkson, *Beyond the plane-parallel and Newtonian approach: Wide-angle redshift distortions and convergence in general relativity*, *JCAP* **1210** (2012) 025, [[arXiv:1205.5221](#)].
- [22] V. Tansella, C. Bonvin, R. Durrer, B. Ghosh, and E. Sellentin, *The full-sky relativistic correlation function and power spectrum of galaxy number counts. Part I: theoretical aspects*, *JCAP* **03** (2018) 019, [[arXiv:1708.00492](#)].
- [23] V. Tansella, G. Jelic-Cizmek, C. Bonvin, and R. Durrer, *COFFE: a code for the full-sky relativistic galaxy correlation function*, *JCAP* **10** (2018) 032, [[arXiv:1806.11090](#)].
- [24] F. Scaccabarozzi, J. Yoo, and S. G. Biern, *Galaxy Two-Point Correlation Function in General Relativity*, *JCAP* **10** (2018) 024, [[arXiv:1807.09796](#)].
- [25] C. Bonvin and R. Durrer, *What galaxy surveys really measure*, *Phys. Rev.* **D84** (2011) 063505, [[arXiv:1105.5280](#)].
- [26] S. Camera, M. G. Santos, and R. Maartens, *Probing primordial non-Gaussianity with SKA galaxy redshift surveys: a fully relativistic analysis*, *Mon. Not. Roy. Astron. Soc.* **448** (2015), no. 2 1035–1043, [[arXiv:1409.8286](#)].
- [27] N. Grimm, F. Scaccabarozzi, J. Yoo, S. G. Biern, and J.-O. Gong, *Galaxy Power Spectrum in General Relativity*, *JCAP* **11** (2020) 064, [[arXiv:2005.06484](#)].
- [28] E. Castorina and E. di Dio, *The observed galaxy power spectrum in General Relativity*, *JCAP* **01** (2022), no. 01 061, [[arXiv:2106.08857](#)].
- [29] M. Foglieni, M. Pantiri, E. Di Dio, and E. Castorina, *Large Scale Limit of the Observed Galaxy Power Spectrum*, *Phys. Rev. Lett.* **131** (2023), no. 11 111201, [[arXiv:2303.03142](#)].
- [30] R. Y. Wen, H. S. Grasshorn Gebhardt, C. Heinrich, and O. Doré, *Exact modeling of power spectrum multipole through spherical Fourier-Bessel basis*, *Phys. Rev. D* **110** (2024), no. 8 083525, [[arXiv:2404.04812](#)].
- [31] F. Semenzato, D. Bertacca, and A. Raccanelli, *The full-sky Spherical Fourier-Bessel power spectrum in general relativity*, [arXiv:2406.09545](#).
- [32] M. Noorikuhani and R. Scoccimarro, *Wide-angle and relativistic effects in Fourier-space clustering statistics*, *Phys. Rev. D* **107** (2023), no. 8 083528, [[arXiv:2207.12383](#)].
- [33] P. Paul, C. Clarkson, and R. Maartens, *Wide-angle effects in multi-tracer power spectra with Doppler corrections*, *JCAP* **04** (2023) 067, [[arXiv:2208.04819](#)].
- [34] S. Jolicoeur, S. L. Guedezounme, R. Maartens, P. Paul, C. Clarkson, and S. Camera, *Relativistic and wide-angle corrections to galaxy power spectra*, *JCAP* **08** (2024) 027, [[arXiv:2406.06274](#)].
- [35] K. Bolejko, C. Clarkson, R. Maartens, D. Bacon, N. Meures, and E. Beynon, *Antilensing: The Bright Side of Voids*, *Phys. Rev. Lett.* **110** (2013), no. 2 021302, [[arXiv:1209.3142](#)].
- [36] D. J. Bacon, S. Andrianomena, C. Clarkson, K. Bolejko, and R. Maartens, *Cosmology with Doppler Lensing*, *Mon. Not. Roy. Astron. Soc.* **443** (2014), no. 3 1900–1915, [[arXiv:1401.3694](#)].
- [37] S. Yahya, P. Bull, M. Santos, M. Silva, R. Maartens, P. Okouma, and B. Bassett, *Cosmological performance of SKA HI galaxy surveys*, *Mon. Not. Roy. Astron. Soc.* **450** (2015), no. 3 2251–2260, [[arXiv:1412.4700](#)].

- [38] M. Kopana, S. Jolicoeur, and R. Maartens, *Multi-tracing the primordial Universe with future surveys*, *Eur. Phys. J. C* **84** (2024), no. 5 491, [[arXiv:2312.12994](#)].
- [39] M. Berti, M. Spinelli, and M. Viel, *Multipole expansion for 21 cm intensity mapping power spectrum: Forecasted cosmological parameters estimation for the SKA observatory*, *Mon. Not. Roy. Astron. Soc.* **521** (2023), no. 3 3221–3236, [[arXiv:2209.07595](#)].
- [40] **Planck** Collaboration, N. Aghanim et al., *Planck 2018 results. VI. Cosmological parameters*, *Astron. Astrophys.* **641** (2020) A6, [[arXiv:1807.06209](#)]. [Erratum: *Astron. Astrophys.* 652, C4 (2021)].
- [41] S. Camera, C. Carbone, C. Fedeli, and L. Moscardini, *Neglecting Primordial non-Gaussianity Threatens Future Cosmological Experiment Accuracy*, *Phys. Rev. D* **91** (2015) 043533, [[arXiv:1412.5172](#)].
- [42] J. Fonseca, S. Camera, M. Santos, and R. Maartens, *Hunting down horizon-scale effects with multi-wavelength surveys*, *Astrophys. J.* **812** (2015), no. 2 L22, [[arXiv:1507.04605](#)].
- [43] G. Jelic-Cizmek, F. Lepori, C. Bonvin, and R. Durrer, *On the importance of lensing for galaxy clustering in photometric and spectroscopic surveys*, *JCAP* **04** (2021) 055, [[arXiv:2004.12981](#)].
- [44] A. Bailoni, A. Spurio Mancini, and L. Amendola, *Improving Fisher matrix forecasts for galaxy surveys: window function, bin cross-correlation, and bin redshift uncertainty*, *Mon. Not. Roy. Astron. Soc.* **470** (2017), no. 1 688–705, [[arXiv:1608.00458](#)].
- [45] S. Rossiter, S. Camera, C. Clarkson, and R. Maartens, *Decoupling Local Primordial non-Gaussianity from Relativistic Effects in the Galaxy Bispectrum*, [[arXiv:2407.06301](#)].